

# Non-thermal pressure in M87 and NGC 1399 gas: X-ray vs. optical potential profiles

E. Churazov,<sup>1,2</sup> W. Forman,<sup>3</sup> A. Vikhlinin,<sup>3,2</sup> S. Tremaine,<sup>4</sup> O. Gerhard,<sup>5</sup> C. Jones<sup>3</sup>

<sup>1</sup> *Max-Planck-Institut für Astrophysik, Karl-Schwarzschild-Strasse 1, 85741 Garching, Germany*

<sup>2</sup> *Space Research Institute (IKI), Profsoyuznaya 84/32, Moscow 117810, Russia*

<sup>3</sup> *Harvard-Smithsonian Center for Astrophysics, 60 Garden St., Cambridge, MA 02138, USA*

<sup>4</sup> *Institute for Advanced Study, Einstein Dr., Princeton, NJ 08540, USA*

<sup>5</sup> *MPI für Extraterrestrische Physik, P.O.Box 1603, 85740 Garching, Germany*

27 November 2018

## ABSTRACT

We compare the gravitational potential profiles of the elliptical galaxies NGC 4486 (M87) and NGC 1399 (the central galaxy in the Fornax cluster) derived from X-ray and optical data. This comparison suggests that the combined contribution of cosmic rays, magnetic fields and micro-turbulence to the pressure is at the level of 7-15% of the gas thermal pressure in the cores of NGC 1399 and M87 respectively, although the uncertainties in our model assumptions (e.g., spherical symmetry) are sufficiently large that the contribution could be consistent with zero. We show that these results are consistent with the current paradigm of cool cluster cores, based on the assumption that AGN activity regulates the thermal state of the gas by injecting energy into the intra-cluster medium. In the absence of any other form of non-thermal pressure support, these upper bounds translate into upper limits on the magnetic field of  $\sim 8$  and  $\sim 20$   $\mu\text{G}$  respectively (evaluated at a distance of  $1'$  in NGC1399 and  $2'$  in M87). The limit of  $\sim 10$ - $20\%$  on the energy density in the form of relativistic protons, applies not only to the current state of the gas, but essentially to the entire history of the intra-cluster medium, provided that cosmic ray protons evolve adiabatically and that their spatial diffusion is suppressed.

**Key words:**

## 1 INTRODUCTION

Both optical and X-ray data are often used to determine the distribution of gravitating mass in galaxies. In the optical band, stars are treated as collisionless particles and the mass distribution is obtained either from the Jeans equations (Binney & Tremaine 1987; Lokas & Mamon 2003) or by finding a distribution of orbits that can explain the observed surface brightness profile and stellar kinematics (e.g., Kronawitter et al. 2000; Thomas et al. 2007). In X-rays, hydrostatic equilibrium is usually assumed for the gaseous atmosphere and the observed density and temperature distributions are then used to evaluate the distribution of gravitating mass (Mathews 1978; Forman, Jones & Tucker 1985; Fukazawa et al. 2006; Humphrey et al. 2006). Ideally both methods should yield identical results, and the mismatch between gravitating masses derived from optical and X-ray data can be used, for example, to measure the contribution of non-thermal particles to the gas pressure. Such non-

thermal particles are directly observed as bubbles of relativistic plasma (e.g. Boehringer et al., 1993). They can also be present in the ICM due to mixing of thermal and relativistic plasma or generated by shocks propagating through the ICM. Below we use the newest Chandra data to compare optical and X-ray data in two giant elliptical galaxies. The angular resolution of Chandra of  $\sim 0''.5$  has brought the X-ray data on a par with optical data and has made it possible to extend the comparison between the kinematics of stars and hot gas from spatial scales of arcseconds up to  $\sim 10'$ . We concentrate on M87 whose core has a moderately disturbed X-ray appearance, and NGC 1399 as an example of a more ‘quiet’ system.

We assume distances of 16 and 19.8 Mpc for M87 and NGC 1399 respectively.

## 2 OBSERVATIONS AND DATA PREPARATION

For the analysis we used Chandra observations (OBSIDS 5826, 5827, 5828, 6186, 7210, 7211, and 7212) taken at a variety of instrument roll angles from February to November 2005 using the ACIS-I detector (CCDs I0-I3) in Very Faint (VF) mode to minimize the background (see Forman et al. 2007a for details). We reprocessed all observations applying the latest CTI and time-dependent gain calibrations (acisD2000-01-29gain\_ctiN0005.fits). We performed the usual filtering by grade, excluded bad/hot pixels and columns, removed cosmic ray ‘afterglows’, and applied the VF mode filtering. We also reprocessed two Faint mode ACIS-S OBSIDS (3717 and 2707) and treated the front (S2) and back (S3) illuminated CCDs independently. We compared the images from the Very Faint and Faint mode observations to verify that no artifacts were introduced near the bright jet by the use of the large  $5 \times 5$  pixel event regions in VF mode. We examined the data for background flaring and found moderate flaring in OBSIDS 3717 and 2707 (the back illuminated CCDs only) for which we excluded approximately half the duration. A typical effective exposure time is  $\sim 500$  ksec. The background files (see Markevitch 2001 for details) were processed in exactly the same manner as the observations.

During 41 ms of the 3.2 s nominal exposure readout of the ACIS CCDs, the chips are exposed to the sky. This results in a small contribution of the source flux, 1.3%, being uniformly re-distributed along the readout direction. This ‘readout artifact’ is most clearly visible when there is a bright point source in the FOV which produces a characteristic readout streak. However, for any emission where a bright region contaminates one of lower surface brightness, this effect must be taken into account. The readout artifact can be accurately subtracted using the technique described by Markevitch et al. (2000). A new event file is generated using the original data by randomizing the CHIPY-coordinate and all sky coordinates and energies are recalculated as if it were a normal observation. The new event file is renormalized by the ratio of the readout time compared to the integration time (41 ms/3.2 s) and then treated exactly as another component of the background. The blank-field background is also renormalized by reducing its integration time by 1.3% to account for this additional subtraction. The nucleus and the brightest jet knot were piled-up in most of observations and the corresponding readout streaks were completely excluded from the analysis.

As the last step of data preparation an additional column was added to each event list. For a given event in the list this column  $\eta$  contains the ratio of the effective area for a photon with a given energy at a given position  $A(E, x_d, y_d)$  normalized by a predefined function of energy  $A_0(E)$ :

$$\eta = A(E, x_d, y_d)/A_0(E), \quad (1)$$

where  $A(E, x_d, y_d)$  includes mirror and detector efficiencies (including non-uniformity of the detector quantum efficiency and the time and spatial dependent contamination on the optical blocking filter). Our data set largely consists of ACIS-I data and a natural choice is to set  $A_0(E)$  to the ACIS-I on-axis effective area. This makes  $\eta$  equal to the vignetting of the mirrors, modified by the (energy dependent)

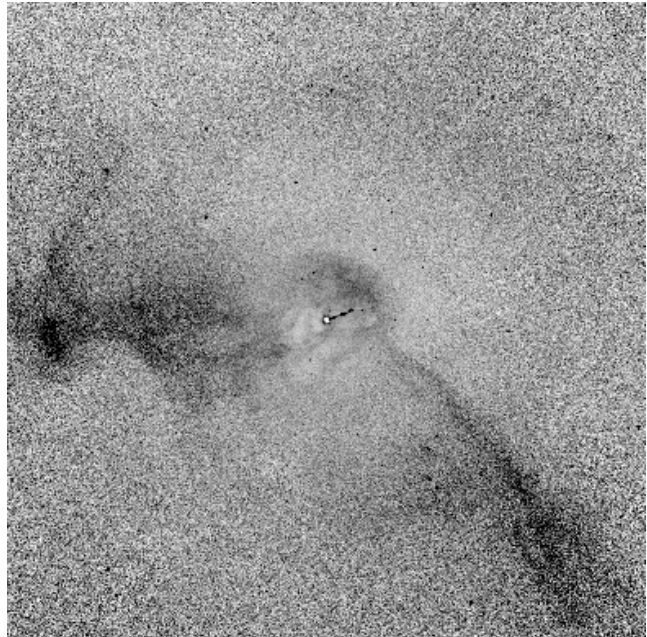


**Figure 1.** Central  $20' \times 20'$  part of the 0.6–2 keV image of M87, divided by the axisymmetric model with surface brightness  $I(R) \propto (1 + (R/r_c)^2)^{1/2-3\beta}$  (here  $R$  is the distance from the M87 nucleus,  $\beta = 0.37$  and  $r_c = 0.2'$ ) to show the structure in the surface brightness more clearly.

variations of quantum efficiency across the detector. The same procedure was repeated with the background data. Finally for each event list we make an exposure map, which accounts for all position dependent, but energy independent efficiency variations across the focal plane (e.g., overall chips geometry, dead pixels or rows, variations of the telescope aspect).

### 2.1 NGC 1399 data

For NGC 1399 we used Chandra data of OBSIDS 319, 4172 and 4174, having a total useful exposure of  $\sim 120$  ksec. The data were cleaned and processed using the same procedures as for the M87 data.

## 3 DEPROJECTION

We use the observations from M87 to describe our method in detail and to explore biases arising from multi-temperature gas components. Such components are clearly visible in M87 (see Fig. 1) and are much less prominent in NGC 1399. Hence, M87 provides the most stringent test of our method.

### 3.1 Broad band

First, using the event lists for all 9 observations, we build an image in the 0.6–2 keV band, centered at the M87 nucleus,  $40'$  on a side and with  $1''$  pixels. For each event with energy in this range the value  $1/\eta$  was added to the corresponding image pixel. The same procedure was applied to the background event lists. An exposure map was generated combining exposure maps for individual event lists.

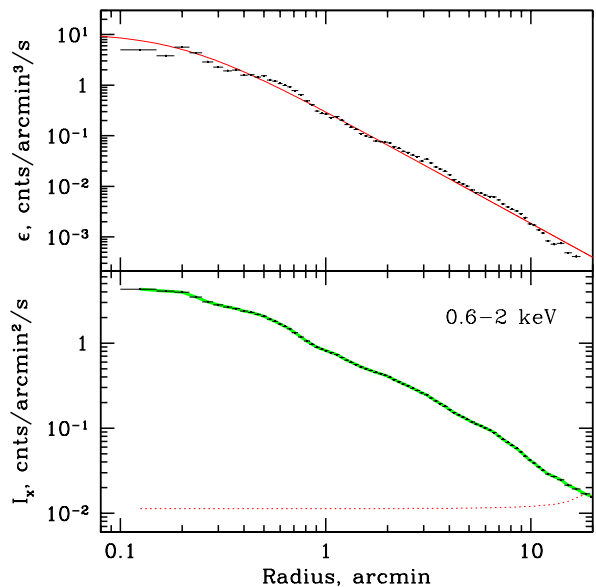


**Figure 2.** M87 surface brightness in the 0.6–2 keV band (lower panel) and the emissivity profile in the same band (upper panel). The solid line in the upper panel shows the function  $(1 + (r/r_c)^2)^{-3\beta}$ , with  $\beta = 0.37$  and  $r_c = 0.2'$ . The thick green solid line in the lower panel shows the projection of the emissivity profile in comparison with the observed surface brightness. The nearly horizontal dotted line is the contribution to the surface brightness in each annulus by the outer gas layers (outside  $19'$ ) where the gas emissivity is assumed to decline as a power law of radius.

A surface brightness profile  $S_{obs}(i)$  (background corrected) calculated from the ‘ $1/\eta$ ’ image in a set of annuli centered at the M87 nucleus is shown in the bottom panel of Fig. 2. The surface brightness is normalized to counts per arcmin<sup>2</sup> per second.

In our deprojection analysis, we follow the approach used in Churazov et al. (2003). We assume spherical symmetry but make no specific assumption about the form of the underlying gravitational potential. For a given surface brightness profile in  $n_a$  annuli, we choose a set of  $n_s$  ( $n_s < n_a$ ) spherical shells with radii  $r(i)$ ,  $i = 1, \dots, n_s$ . The gas emissivity  $\mathcal{E}$  is assumed to be uniform inside each shell. The gas emissivity for radii larger than  $r(n_s)$  is assumed to decline as a power law of radius:  $\mathcal{E} = \mathcal{E}_{out} r^{-6\beta_{out}}$ , where  $\beta_{out}$  is a parameter. In our analysis  $r(n_s)$  was set to  $19'$  and  $\beta_{out} = 2/6$ . In practice we are mostly working with the data inside a  $10'$  circle and the choice of  $\beta_{out}$  and the outer radius do not affect the results.

The expected surface brightness can then be written as a projection of emissivities in each of the  $n_s$  shells plus a contribution from the outer layers ( $r > r(n_s)$ ):

$$S(j) = \sum_{i=1}^{n_s} P(i, j) \mathcal{E}(i) + P_{out}(j) \mathcal{E}_{out}, \quad (2)$$

where  $\mathcal{E}(i)$  is the emissivity of a given shell,  $\mathcal{E}_{out}$  is the emissivity of the outer layers of the gas at  $r = 1$ ,  $P(i, j)$  and

$P_{out}(j)$  are the projection matrix/vector from our set of shells into our set of annuli. A simple analytical expression for  $P(i, j)$ , which is a function of the geometry only, is given by McLaughlin (1999).

Deprojection can then be reduced to a simple least squares problem – what set of emissivities in our set of shells (together with the emissivity normalization  $\mathcal{E}_{out}$  for the outer layers) provides the best description of the observed surface brightness:

$$\chi^2 = \sum_j [S(j) - S_{obs}(j)]^2 / \sigma(j)^2 = \min, \quad (3)$$

where  $\sigma(j)$  is the error associated with the surface brightness in annulus number  $j$ . In our analysis, we use modified errors  $\sigma(j)^2 = \sigma_{stat}(j)^2 + \delta^2 \times S_{obs}(j)^2$ , where  $\sigma_{stat}(j)$  is the statistical error associated with the Poissonian noise in the observed image and background and  $\delta \sim 0.1$ . This was done to avoid the situation where a few annuli with the best statistics completely dominate the  $\chi^2$ . In practice for the M87 dataset, the choice of  $\delta$  does not affect the results. As usual the differentiation of this relation with respect to  $\mathcal{E}(i)$  and  $\mathcal{E}_{out}$  yields a system of linear equations, which can easily be solved. In the cases considered below, the solution of eq. (3) is unique, once the parameter  $\beta_{out}$  is fixed. The properties of the inverse matrix  $P^{-1}$  (in particular an error enhancement when the ratio of maximal to minimal eigenvalues of  $P$  is large) can easily be controlled by making the spherical shells broader. A practical recipe for the choice of shells/annuli radii will be described elsewhere.

The emissivity of each shell can then be evaluated as an explicit linear combination of the observed quantities:

$$\mathcal{E}(i), \mathcal{E}_{out} = \sum_{j=1, n_a} P^{-1}(j, i) S_{obs}(j) \quad (4)$$

Since the whole procedure is linear, the errors in the observed quantities can be propagated straightforwardly. Shown in Fig. 2 (upper panel) is the set of gas emissivities in the 0.6–2 keV band derived from the surface brightness profile. The forward convolution of this set of emissivities with the projected matrix  $P(i, j)$  (blue line in the lower panel of Fig. 2) accurately reproduces the observed surface brightness profile.

### 3.2 Deprojected spectra

Note that with our definition of  $\eta$  the projection matrix  $P(i, j)$  does not depend on energy. Indeed all energy/position dependent factors are already corrected for when we make the  $1/\eta$  image instead of a usual image constructed from raw counts without any weights. We do lose some of the sensitivity with this  $1/\eta$  procedure, but not much as long as the variations of  $1/\eta$  across the region used for spectrum extraction are not large.

Since  $P(i, j)$  does not depend on energy, the deprojection of a surface brightness profile in any energy band would look like eq. (4) with exactly the same  $P^{-1}(j, i)$ . Thus we can accumulate a set of ‘ $1/\eta$ ’ spectra (corrected for background and readout) for each of the  $n_a$  annuli, and apply eq. (4) to determine the emissivities of each shell in each of the ACIS energy channels.

The resulting spectra were fitted in XSPEC V12 (Arnaud 1996) with a single-temperature optically thin plasma

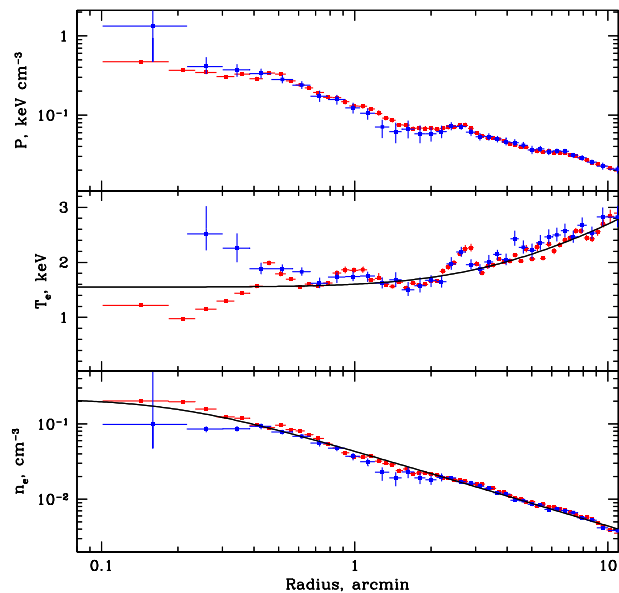


**Figure 3.** Radial profiles of deprojected parameters in M87. The parameters were obtained using a single temperature APEC fit (with fixed low energy absorption and redshift) to the deprojected spectra for a set of spherical shells centered on M87. The red and blue points correspond to the best-fitting parameters for the 0.6–9 keV and 2.5–9 keV energy bands respectively. Simple analytical approximations for the density and temperature are shown with the solid lines. The uppermost panel shows the gas pressure evaluated as  $P = nT = 1.91n_eT$ , where  $n_e$  and  $T$  are the best-fitting electron density and temperature.

emission model as implemented in the APEC code (Smith et al. 2001). The low energy photoabsorption was fixed at the Galactic value  $N_H = 2.54 \times 10^{20} \text{ cm}^{-2}$  (Dickey & Lockman 1990) and the redshift was fixed at the optically determined redshift of M87:  $z = 0.00436$  (e.g., Smith et al. 2000). The gas temperature, heavy metal abundance and normalization were free parameters of the model. The deprojected spectra were generated in narrow (14.6 eV) energy bins and used in XSPEC without any further grouping. In order to avoid bias towards lower temperatures, which is present when the number of counts per spectral bin at high energies becomes less than  $\sim 10$ –20, the statistical errors were evaluated from the smoothed spectra (see Churazov et al. 1996 for details).

The electron density was derived from the normalization of the spectra, fixing the proton to electron ratio to 0.83 and taking into account the distance to M87. The resulting spectral parameters are plotted in Fig. 3 as a function of distance from the center of M87. Red and blue points correspond to the best-fitting model parameters in the 0.6–9 and 2.5–9 keV bands respectively. This choice of two energy bands for spectral fitting is motivated on the following grounds: the broader band maximizes the statistical significance of the results, while the harder band provides a verification of the magnitude of biases which might arise when a one-temperature model is applied to a spectrum with multiple temperature components (e.g., Buote 2000).

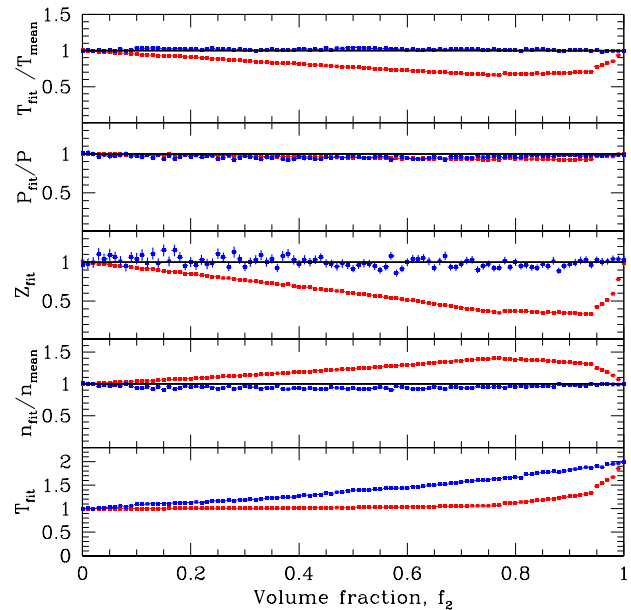


**Figure 4.** ‘Biases’ in a two-temperature plasma versus volume fraction of the hotter component. The fake Chandra spectra representing a mixture of  $kT_1 = 1$  and  $kT_2 = 2$  keV plasmas in pressure equilibrium were fitted with a one-temperature model in the 0.6–9 and 2.5–9 keV bands (red and blue points respectively). The four panels from bottom to top show i) the best-fitting gas temperature, ii) the ratio of best-fitting gas density to the true mean density, iii) gas metallicity, iv) gas pressure  $P_{fit} \equiv n_{fit}T_{fit}$ , v) the ratio of the measured value  $P_{fit}/n_{fit} \equiv T_{fit}$  to the true value  $P/n_{mean} \equiv T_{mean}$ ; here  $n_{mean}$  is the volume averaged plasma density (eq. 5). This quantity characterizes the bias in measuring the gravitating mass or the potential from the hydrostatic equilibrium equation.

To assess the magnitude of possible biases when fitting the multi-temperature plasma in the Chandra band with a one-temperature model, we generated a sequence of fake spectra representing a mixture of  $kT_1 = 1$  and  $kT_2 = 2$  keV plasmas in pressure equilibrium, with a varying volume fraction  $f_2$  of the harder component. The abundance of heavy elements was set to solar for both components, and  $N_H$  and redshift were fixed to the M87 values. The on-axis ACIS-I response was used. We then applied to the simulated spectra the same one-temperature model as we did for the real M87 data. The resulting spectral parameters are shown in Fig. 4: temperature, density, metallicity, pressure  $P_{fit} \equiv n_{fit}T_{fit}$ , and the ratio of the measured value  $P_{fit}/n_{fit} \equiv T_{fit}$  to the true value  $P/n_{mean} \equiv T_{mean}$ ;

$$n_{mean} = n_1 \times (1 - f_2) + n_2 \times f_2 \quad (5)$$

is the volume averaged plasma density and  $n_1$  and  $n_2$  are the plasma densities of the cooler and hotter phases respectively (evaluated as 1.91 times the electron density  $n_e$ ). The quantity  $T_{fit}/T_{mean} - 1$  characterizes the bias in measuring gravitating mass or the potential from the hydrostatic equilibrium equation. The red and blue points correspond to the best-fitting parameters derived from the 0.6–9 and 2.5–9 keV bands respectively. For the 0.6–9 keV band, even

a very small volume fraction of the cooler component causes the best-fitting temperature and metallicity to drop sharply, while the density rises (red points in Fig. 4). For the 2.5–9 keV band, the density is, on the contrary, very close to the mean value. This conclusion is of course sensitive to the particular choice of  $T_1$  and  $T_2$  and to the effective area of the instrument. In general, one expects the best-fitting temperature in the broad band to be more biased towards lower values compared to the hard band. It is possible therefore to use the differences in the best-fitting values obtained in two energy bands as an indicator of strong departures from a single-temperature plasma. From Fig. 3 it is clear that the best-fitting values in the 0.6–9 and 2.5–9 keV bands differ strongly inside the inner  $0'.4$ , while outside this radius, the results agree well. Of course even a reasonable agreement between the spectral results in two bands does not guarantee that the spectrum is fully described by a one-temperature model. This agreement nevertheless suggests that outside  $0'.4$  our spectral results are not strongly biased. On the other hand, the region inside  $0'.4$  is characterized by very strong departures from spherical symmetry and by the presence of cool and hot gas structures. Given the magnitude of the expected biases the results for this region should be taken with caution.

From Chandra and XMM-Newton observations we know that the gas temperature in the X-ray bright features co-spatial with the extended radio bright ‘arms’ is lower than that of the typical intra-cluster medium (ICM) temperature at the same distance from the center (e.g., Belsole et al. 2001; Matsushita et al. 2002; Forman et al., 2005). These regions are clearly seen in Fig. 1 as dark and extended structures to the east and the south-west of the nucleus. To test whether these structures dramatically affect our final result (e.g., the mass/potential profile, discussed below) we also fit the data excluding those regions containing the brightest parts of the arms. We use the spectral fits to this ‘trimmed’ data-set in the next section to verify the robustness of our results.

Analytical approximations to the best-fitting values of  $n_e(r)$  and  $kT(r)$  over the range of radii from  $\sim 0.5'$  to  $\sim 5'$  are given below:

$$n_e = \frac{0.22}{\left[1 + \left(\frac{r}{r_c}\right)^2\right]^{\frac{3}{2}\beta}} \text{ cm}^{-3}, \quad (6)$$

where  $\beta = 0.37$  and  $r_c = 0.2'$  (or 0.93 kpc).

$$kT = 1.55 \times \left[1 + \left(\frac{r}{2.2'}\right)^2\right]^{0.18} \text{ keV}. \quad (7)$$

These approximations are shown in Fig. 3 by the black solid lines.

## 4 POTENTIAL

We first derive the gravitational potential for M87, including a detailed discussion of the method which we then apply to the data for NGC 1399.

**Table 1.** Data used to derive potential.

Regions	Energy band	Color in Fig. 5
0-360° annuli	0.6–9 keV	blue
0-360° annuli, excluding ‘arms’	0.6–9 keV	red
0-360° annuli, excluding ‘arms’	2.5–9 keV	green

### 4.1 M87

Assuming that the gaseous atmosphere of M87 is in hydrostatic equilibrium:

$$\frac{1}{\rho} \frac{dP}{dr} = -\frac{d\varphi}{dr}, \quad (8)$$

where  $\rho$  is the gas density,  $P = P(r)$  is the pressure and  $\varphi$  is the gravitational potential. Thus

$$\varphi = -\int \frac{1}{\rho} \frac{dP}{dr} dr, \quad (9)$$

If the pressure is solely due to the thermal gas pressure, then  $P = nkT$  and  $\rho = \mu m_p n$ , where  $\mu$  is the mean atomic weight of the gas particles,  $m_p$  is the proton mass, and  $n = n(r)$  is the total particle density. Then (assuming that  $\mu$  does not vary with radius) the potential  $\varphi$  is:

$$\varphi = -\frac{k}{\mu m_p} \left[ \int T \frac{d \ln n}{dr} dr + T \right] + C, \quad (10)$$

where  $C$  is an arbitrary constant. Below we will use the value of the potential relative to a given reference radius  $r_{ref} = 5'$  (23.25 kpc), i.e.,  $\varphi(5') = 0$ . Note that the eq. (10) depends only on the measured quantities  $n(r)$  and  $T(r)$ . Furthermore, eq. (10) does not depend explicitly on radius  $r$  (only through  $n(r)$  and  $T(r)$ ) or on the absolute normalization of the gas density. This in particular means that the assumed distance to M87 does not affect the calculated potential as long as it is expressed as a function of angular distance from the nucleus. Thus  $\varphi$  can be easily evaluated using the densities and temperatures derived from the deprojected X-ray spectra. Unlike the expression for gravitating mass, which explicitly depends on the spatial derivatives of the observed quantities, the change of the potential  $\Delta\varphi$  between two radii  $r_1$  and  $r_2$  depends primarily on the gas densities at two radii and on the mean gas temperature. Thus, in the case of isothermal gas,  $\Delta\varphi \propto T \ln(n(r_2)/n(r_1))$  which is of course a direct consequence of the Boltzmann distribution. This makes the calculation of  $\Delta\varphi$  (and associated errors) very simple and robust.

Below we will denote the potential derived from X-ray data as  $\varphi_X$  to distinguish it from the true potential  $\varphi$  or from the potential  $\varphi_{opt}$  derived from optical data.

In Fig. 5 we show three versions of  $\varphi_X$  derived from the Chandra data for M87. Each of the three shaded ‘curves’ corresponds to different subsets of data and/or different energy bands used for spectral fitting, as indicated in Table 1. The vertical width of each of the color curves in Fig. 5 corresponds to the 67% statistical uncertainty.

All three methods lead to estimates of  $\varphi_X(r)$  that are consistent with each other within statistical uncertainties. The potential derived from the data in the 2.5–9 keV band has the largest statistical errors, but as discussed above, the spectral parameters might be less biased in this band, compared to the broader 0.6–9 keV band. We note here that

departures from spherical symmetry are obvious from Fig. 1 and we cannot expect the spectral parameters (or potential profiles) to be perfectly consistent with each other.

For comparison to the X-ray derived gravitational potentials, we show in Fig. 5, with the black lines, two estimates of the gravitational potential that are derived from the optical data. The dashed line shows the potential derived by Wu & Tremaine (2006) using a sample of 161 globular clusters in M87. The mass profile in this model is a power law function of radius  $M(r) = 2.3 \times 10^{10} M_{\odot} (r/\text{kpc})^{1.36}$ . This mass distribution is most accurately determined near  $r = 30$  kpc but Wu & Tremaine estimate that the relative error in  $M(r)$  is less than 40% for  $17 \text{ kpc} < r < 90 \text{ kpc}$  (or  $3.7' < r < 19'$ ). The error in the potential is substantially smaller since it is determined by the integral of the mass distribution,  $\phi_{opt} = \int_{r_{ref}}^r GM(r)dr/r^2$ . The potential in the inner few arcminutes is only weakly constrained since this model does not use any information on stellar kinematics. The thick solid line in Fig. 5 is the best-fitting model to the star and globular-cluster kinematics in M87 from Romanowsky & Kochanek (2001, their §4.2; RK01 below). This model (NFW2 in their Table 2) has a mass profile that is the sum of an NFW profile (Navarro, Frenk & White, 1996) from a dark halo and a stellar component, derived from the M87 optical surface brightness under the assumption of a constant stellar mass-to-light ratio. In terms of the likelihood, this is the most probable model among those considered by RK01. This model agrees reasonably well with the X-ray derived potential apart from a few clear wiggles in  $\varphi_X(r)$ , which we discuss in Section 5.4.

We assume below that the NFW2 model of RK01 provides the best description of the M87 optical data in the range of radii from a few arcseconds to a few arcminutes from the M87 center and we assume that it represents the true potential of the galaxy.

## 4.2 NGC 1399

The X-ray potential  $\varphi_X(r)$  derived from Chandra data for NGC 1399 is shown in Fig. 6 with the blue curve. The potential is set to zero at  $1'.5$ . In X-rays the core of NGC 1399 looks less disturbed than M87 and the resulting  $\varphi_X(r)$  is much smoother than for M87. For comparison  $\varphi_{opt}(r)$  based on the model of Kronawitter et al. (2000) is shown with the black solid line. As in the case of M87 there is good agreement of  $\varphi_X(r)$  and  $\varphi_{opt}(r)$  over the region where X-ray and optical data are available.

The optical potential  $\phi_{opt}$  for NGC 1399 was derived from absorption-line kinematic data, as described in Saglia et al. (2000). These authors constructed spherical models for the galaxy in a sequence of gravitational potentials, composed of the potential of the luminous stars and various optional quasi-isothermal dark halo potentials. The potential of the stars was based on the deprojected luminosity distribution and the assumption of constant mass-to-light ratio. For each of these potentials, the non-parametric distribution function  $f(E, L2)$  was found that gave the best fit to the kinematic data; here  $E$  and  $L$  denote energy and total angular momentum. The  $\Delta\chi^2$  values of the various models then determined the boundaries of the confidence region for the halo potential parameters. Similar models, based on a

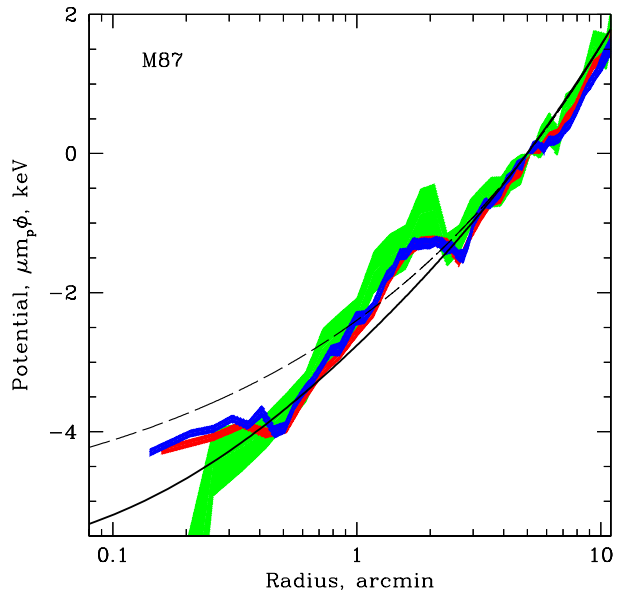


**Figure 5.** Derived potential  $\varphi_X(r)$  using the 0.6–9 keV band (blue), the same excluding ‘cool arms’ (red), the same in the 2.5–9 keV band (green) – see Table 1. Black curves - potentials  $\varphi_{opt}(r)$  derived from optical data: Wu & Tremaine (2006) - dashed line; Romanowsky & Kochanek (2001), NFW2 model - thick solid line. All curves are normalized to zero at  $5'$ .

larger basis of distribution functions and potentials, were constructed by Kronawitter et al. (2000). The Kronawitter et al. models are plotted in Fig. 6 and span the 95% confidence range within their expanded set of potentials. The true confidence range based on non-parametric potentials is likely to be somewhat larger; however, it is not straightforward to determine.

## 5 EFFECTS OF MAGNETIC FIELDS, COSMIC RAYS, AND MICRO-TURBULENCE

The good agreement of the optical and X-ray data, found in the previous section, suggests that hydrostatic equilibrium is satisfied reasonably well in M87 and NGC1399. This conclusion contrasts with that of Diehl & Statler (2007) who have argued recently that hydrostatic equilibrium of the X-ray gas in elliptical galaxies is “the exception rather than the rule” and “X-ray-derived radial mass profiles may be in error by factors of order unity”. While our sample consists of only two objects, one of them - NGC1399 - is also included in the Diehl & Statler (2007) sample and in their analysis it is apparently among the candidates that are far from hydrostatic equilibrium. We note that (i) Diehl & Statler’s conclusion is based mainly on differences in the isophotal shapes of the stars and the X-ray gas, and this comparison is much more sensitive to small-scale deviations from equilibrium than the spherically averaged hydrostatic equilibrium equations used here; (ii) the use of surface brightness images as a proxy for the pressure distribution is prone to

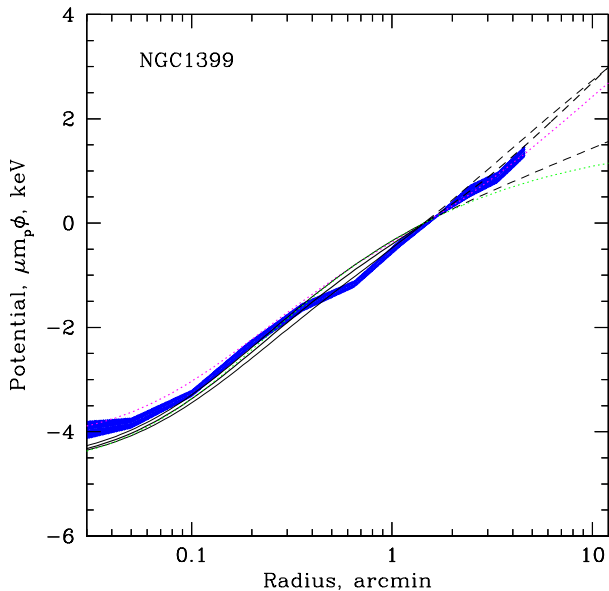


**Figure 6.** Derived potential  $\varphi_X(r)$  for NGC 1399 using 0.6–9 keV band for 0–360° annuli (blue curve). The thick black solid line shows the potential  $\varphi_{opt}(r)$  derived from optical data of Kronawitter et al. (2000), while thin black lines show  $\pm 2\sigma$  limits. Outside the range of radii covered by the optical data ( $r < 1.62'$ ), the extrapolation of the potential is shown by dashed lines. The green curve is the ‘stars-only’ model from Kronawitter et al. (2000). The magenta line shows the optical potential  $\varphi_{opt}(r)$  multiplied by 0.9. All curves are normalized to zero at  $1'.5$ .

various biases in the multi-temperature plasma as shown in Section 4 (see Fig.4); (iii) our approach of using the gravitational potential change over a large span of radii, rather than gravitating mass, emphasises the global change of pressure rather than the local curvature of the radial dependence of pressure. We believe that the close agreement of the potential profiles  $\phi_X(r)$  and  $\phi_{opt}(r)$  obtained in the previous section would be an improbable coincidence if hydrostatic equilibrium were not approximately valid and we will verify this for a larger sample of elliptical galaxies in future work.

We now consider how magnetic fields, cosmic rays and micro-turbulence would affect the potential  $\varphi_X(r)$  derived from the X-ray data. We keep the hydrostatic equilibrium assumption (eq. 9), but we now allow the pressure or density derived from X-ray analysis to differ from the true  $P$  and  $\rho$  entering eq. (9).

### 5.1 Uniform medium

Let us first keep the assumption that the X-ray emitting gas is uniform within each spherical shell, but assume that this gas provides only part of the total pressure. The rest of the pressure is provided by a component that is ‘invisible’ in X-rays (e.g., cosmic rays), which is also uniformly distributed through the volume of each shell. Here and below we assume (unless stated otherwise) that the pressure is isotropic and the atmosphere is in hydrostatic equilibrium, with the ther-

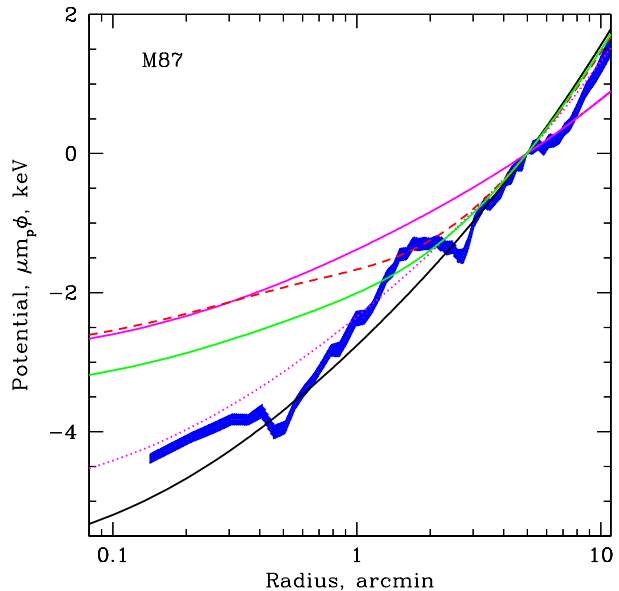


**Figure 7.** Expected potential  $\varphi_X$  that would be derived from X-ray observations if non-thermal pressure were present. We assumed that the true potential is the NFW2 model of RK01 (thick black solid line). Other curves:  $\varphi_X$  from eq. (11) for  $f_g = \text{const} = 0.5$  and  $0.85$  (magenta solid and dotted lines respectively) and for  $f_g$  given by eq. (12) (red dashed line). The  $\varphi_X$  derived from eq. (13) for  $f_g$  given by eq. (12) is shown by the green line.

mal gas ‘mechanically’ coupled to other components. We define the fraction of the pressure due to thermal gas as  $f_g = f_g(r)$ . Then the pressure derived from X-ray data will be  $nkT = f_g P$ , where  $P$  is the true total pressure,  $n$  and  $T$  are the density and temperature measured from X-ray data. If we further assume that only thermal gas contributes to the mass density, then  $\rho = \mu m_p n$  will be correctly determined from the X-ray analysis. The temperature is also assumed to be determined correctly. Substituting  $f_g P$  instead of  $P$  into eq. (9), we can easily express  $\varphi_X(r)$  through the true potential  $\varphi(r)$  and other gas parameters:

$$\varphi_X = \int f_g d\varphi - \frac{k}{\mu m_p} \int T \frac{d \ln f_g}{dr} dr. \quad (11)$$

If  $f_g$  does not depend on radius then obviously  $\varphi_X = f_g \varphi$ . Shown in Fig. (7) is  $\varphi_X$  from eq. (11) for  $f_g = \text{const} = 0.5$  and  $0.85$  (magenta solid and dotted lines respectively) and for

$$f_g = [1 + (r/1')^2]/[2 + (r/1')^2] \quad (12)$$

(red dashed line). The latter case illustrates the situation when gas pressure dominates at large radii ( $f_g = 1$ ), but declines to 50% ( $f_g = 0.5$ ) in the core. In these calculations we used  $\varphi$  based on the NFW2 model of RK01 and the analytic approximation of temperature given by eq. (7). The curves for  $f_g = 1$  and  $f_g = 0.85$  fit the X-ray data reasonably well but the other models are excluded. For NGC 1399 the  $\varphi_X$  and  $\varphi_{opt}$  closely follow each other and  $f_g$  smaller than 0.9

(dotted magenta line in Fig. 6) would lead to a substantially worse fit between  $\varphi_X$  and  $\varphi_{opt}$  than  $f_g = 1$ .

## 5.2 Micro-turbulence

If small scale and isotropic turbulent motions are present in the medium then the impact on  $\varphi_X$  can be evaluated similar to the case considered in the previous section. The quantity  $1 - f_g$  characterizes the contribution of turbulent motions to the pressure (or energy density) of the medium.

## 5.3 Patchy medium

We now assume that the medium is not uniform, but patchy, with a volume fraction  $f_g$  filled with the thermal gas. The remaining volume fraction is completely devoid of thermal gas and is occupied by bubbles of cosmic rays and magnetic fields. Both phases are assumed to be in pressure equilibrium and coupled together. If, doing X-ray deprojection, one still assumes that the gas is uniform (as we did above), the derived gas density will be lower than the true gas density in the gas patches and higher than the mean volume density:  $\rho_{obs} = \rho_{gas} \sqrt{f_g} = \rho_{mean} / \sqrt{f_g}$ . The pressure derived from the X-ray analysis will be modified accordingly. For this case, the potential is:

$$\varphi_X = \int f_g d\varphi - \frac{1}{2} \frac{k}{\mu m_p} \int T \frac{d \ln f_g}{dr} dr. \quad (13)$$

The X-ray potential  $\varphi_X$  derived from eq. 13 for  $f_g$  given by eq. (12) is shown in Fig. 7 by the green line.

We note here that a similar problem (the impact of bubbles on the observed gas distribution) has been recently considered in Nusser & Silk (2007).

## 5.4 Sound waves and shocks

The presence of sound and shock waves makes our assumption of hydrostatic equilibrium invalid. At any given location the potential derived from X-ray data can be either underestimated or overestimated, depending on the sign of the pressure gradient in the wave. Forman et al. (2005, 2007a) identified in the X-ray data a number of quasi-spherical features around M87 which are plausibly caused by shock waves produced by an unsteady outflow of relativistic plasma from the supermassive black hole at the center of M87. These shock candidates are located exactly where we see wiggles in the potential (Fig. 7). This is not surprising since, in a spherical shock propagating from the center of the galaxy, the pressure first increases sharply inwards at the front and then decreases in the rarefaction region behind the shock. The potential derived from the X-ray analysis (see eq.10) will have a ‘dip’ at the position of the shock front and it will then recover from this dip over the rarefaction region. To illustrate such behavior we simulated a spherical shock in the atmosphere of M87 and calculated the potential  $\varphi_X$  which would be derived from X-ray data, corresponding to these simulations. Fig. 8 shows the true potential, assumed in the simulations, with the black line, while the blue line shows  $\varphi_X$  calculated for a Mach 1.2 shock located 2.7’ from the nucleus (see Forman et al. 2007a,b for details of the shock parameters and the simulations).

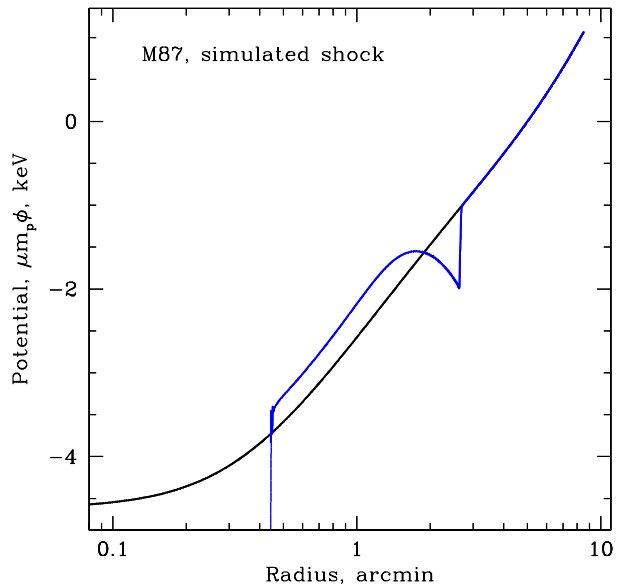


**Figure 8.** Potential ( $\varphi_X$  - blue line) derived using eq. 10 from simulated density and temperature profiles. In these simulations a powerful explosion (with total energy a few  $10^{57}$  erg) at the center of the galaxy drove a shock through the ICM. The data shown in the figure correspond to the moment of time when the shock of Mach number  $\sim 1.2$  is located  $\sim 2.7'$  from the nucleus, the observed radius of the main shock in M87. The true potential is shown with the black line.

For weak shocks/sound waves which are well localized in space (e.g., weak compression waves)  $\varphi_X$  will be affected only in the region where the wave is present, while  $\Delta\varphi_X = \varphi_X(r_2) - \varphi_X(r_1)$  over the range of radii from  $r_1$  to  $r_2$  which covers the entire perturbation will not be affected. Therefore, weak and localized perturbations do not affect the global change of  $\varphi_X$ .

## 5.5 Non-luminous gas

In Sections 5.1, 5.2, 5.3 we have assumed that there is an ‘invisible’ (in X-rays) component contributing to the pressure. As a result, the derived potential  $\varphi_X$  was flatter than the true potential. We can also assume that there is an X-ray ‘invisible’ gas component which contributes to the mass density and has a small filling factor. For example, a cool gas phase with temperature below ‘observable’ X-ray values but coupled to the X-ray emitting phase (e.g., by magnetic fields) would be a simplest example. The  $\varphi_X$  derived from (9) will be simply:

$$\varphi_X = \int f_m d\varphi, \quad (14)$$

where  $f_m = \frac{\rho}{\rho_X}$  is the ratio of total mass density to the mass density derived from the X-ray analysis. In this case  $f_m > 1$  and the X-ray derived potential will be steeper than the true potential.

## 5.6 Non-spherical models

We have assumed that the gravitational potential in both M87 and NGC 1399 is spherical. The ellipticity of the optical isophotes of M87 is near zero at the center, rising to 0.4 at  $10'$ , while the ellipticity of the X-ray isophotes outside  $5'$  is 0.1–0.15, with the same position angle (Böhringer et al. 1997). The ellipticity of the optical isophotes of NGC 1399 is about 0.1 out to  $10'$  (Dirsch et al. 2003). The X-ray image of NGC1399 looks more disturbed than the optical image and has an ellipticity of 0.34 at the effective radius of the galaxy (Diehl & Statler 2007). The shapes of the X-ray emitting gas and the stellar distribution need not be the same since the velocity-dispersion tensor of the stars is not necessarily isotropic.

Thus both galaxies exhibit a modest level of non-axisymmetry in their X-ray and optical isophotes, which is unlikely to seriously compromise our mass estimates. A more serious concern is that the actual deviations from spherical symmetry may be larger than the observations indicate if the galaxy is an approximately axisymmetric system that is viewed pole-on.

The effects of a non-spherical potential on X-ray estimates of mass or potential have been modelled by Piffaretti et al. (2003). Although Piffaretti et al. were concerned with clusters of galaxies, their results should apply to galaxies as well. They found that if (i) the galaxy potential is axisymmetric and viewed pole-on; (ii) its mass is estimated from the temperature and distribution of hot gas on the assumption that the potential is spherical; then if the axis ratio of the potential is varied within plausible limits (typically  $\pm 40\%$ ), the derived mass within a spherical radius is typically in error by only a few per cent.

The effects of a non-spherical potential on optical estimates of mass are more difficult to model. The simplest approach is based on the tensor virial theorem (e.g., Binney & Tremaine 1987). If (i) an axisymmetric one-component self-gravitating stellar system is viewed pole-on; (ii) the density of stars in the system is constant on spheroids of eccentricity  $e$ ; (iii) the mass of the system is estimated using the virial theorem for spherical systems; then the derived mass will exceed the actual mass by a factor  $f$ , where

$$f(e) = \begin{cases} 3 \frac{1-e^2}{e^2} \left( \frac{1}{\sqrt{1-e^2}} - \frac{\sin^{-1} e}{e} \right) & \text{oblate systems} \\ 3 \frac{\sqrt{-e^2}}{e^2} \left( \frac{1}{2e} \log \frac{1+e}{1-e} - 1 \right) & \text{prolate systems,} \end{cases} \quad (15)$$

where  $e = \sqrt{1 - b^2/a^2}$  and  $b/a$  is the axis ratio. For a plausible range of axis ratio, say  $0.5 < b/a < 1$ ,  $f$  varies only between 0.79 (most oblate) and 1.04 (most prolate), suggesting that the error in the optical potential due to asphericity is likely to be small. It should also be stressed that viewing a very oblate or prolate system nearly pole-on is rather unlikely, and that substantial errors due to asphericity are likely to affect the optical and X-ray estimates of the potential in different ways, so the close agreement seen in Figs. 5 and 6 would be a coincidence.

## 6 DISCUSSION

In Fig. 9 the potential derived from X-ray data is plotted against the potential derived from optical data for M87

and NGC 1399 (red shaded areas). If the assumptions used when deriving the potentials are correct, then one expects to find  $\varphi_X = \varphi_{opt}$  (shown with the dashed lines). If cosmic rays, magnetic fields or micro-turbulence contribute to the pressure in the X-ray emitting gas, then  $\varphi_X$  will be more shallow, i.e.,  $\varphi_X = a\varphi_{opt}$ , where  $a < 1$ . A formal linear fit  $\varphi_X = a\varphi_{opt} + b$  to observations is shown in Fig. 9 with the thick solid line. The values of  $a$  are 0.85 and 0.93 for M87 and NGC 1399, respectively. Taken at face value this means that non-thermal contribution to pressure amounts to 15% and 7% in M87 and NGC 1399 respectively. These values characterize the non-thermal contribution to pressure averaged over the range of radii from  $0'.5$  to  $12'$  in M87 and from  $3'$  to  $5'$  in NGC 1399. Given that systematic uncertainties are present in the data (e.g., due to the shock in M87) it is difficult to provide a reliable estimate of the uncertainty associated with this value. If one adopts a more conservative approach of upper limits (rather than measurements) on the non-thermal pressure components then these limits are  $\sim 10\%$  and  $\sim 20\%$  for NGC 1399 and M87 respectively (see Fig. 9).

Errors in the optical potential profile could also contribute to the observed difference. In both galaxies, uncertainties arise from the assumption of spherical symmetry, the restriction to a particular family of parametric halo potentials in the dynamical modeling, and possible systematic errors in deriving the line-of-sight velocity distribution from the observed spectra. These uncertainties are difficult to estimate. Thomas et al. (2007) have investigated the uncertainties in the inferred circular velocity curves for a sample of Coma cluster ellipticals which they studied with axisymmetric dynamical models. In these galaxies, the central mass density is dominated by the luminous matter, independent of the dark matter halo profile used; thus the circular velocities inside  $\simeq 0.5R_e$  are accurately determined, within  $\simeq 5\%$ . At two effective radii, the uncertainties in the inferred circular velocities for their galaxies are  $\simeq 15\%$ . The measurement errors of the observed kinematics in NGC 1399 (Saglia et al. 2000) are smaller than in the Coma ellipticals. However, these data are along only one long slit. Hence, we would expect somewhat smaller uncertainties in NGC 1399. However, note that errors  $\phi_{opt} - \phi_{true}$  in the inferred optical potential profiles are likely to be more slowly varying functions of radius than the variations in  $\phi_X - \phi_{opt}$  seen in Fig. 6.

The  $\varphi_X - \varphi_{opt}$  difference characterizes the combined contribution of all components of non-thermal pressure and the modelling uncertainties of the respective datasets. Under the assumption that modelling uncertainties do not dominate and that the contributions of individual components of the non-thermal pressure all have the same sign, the measured values can be converted to upper limits. For example, fractions of non-thermal pressure support of 15 and 7% in M87 and NGC 1399 respectively, translate into upper limits on the magnetic field of  $\sim 20$  and  $\sim 8 \mu\text{G}$  respectively (evaluated at a distance of  $2'$  in M87 and  $1'$  in NGC 1399).

The central region of M87 is a classic example of a cooling flow – a region where gas radiative losses are high and an external source of energy is required if one wants to have a quasi-steady state without large net cooling of the gas, as indicated by the recent XMM-Newton RGS data (e.g., Peterson et al. 2003). A plausible source of energy for gas

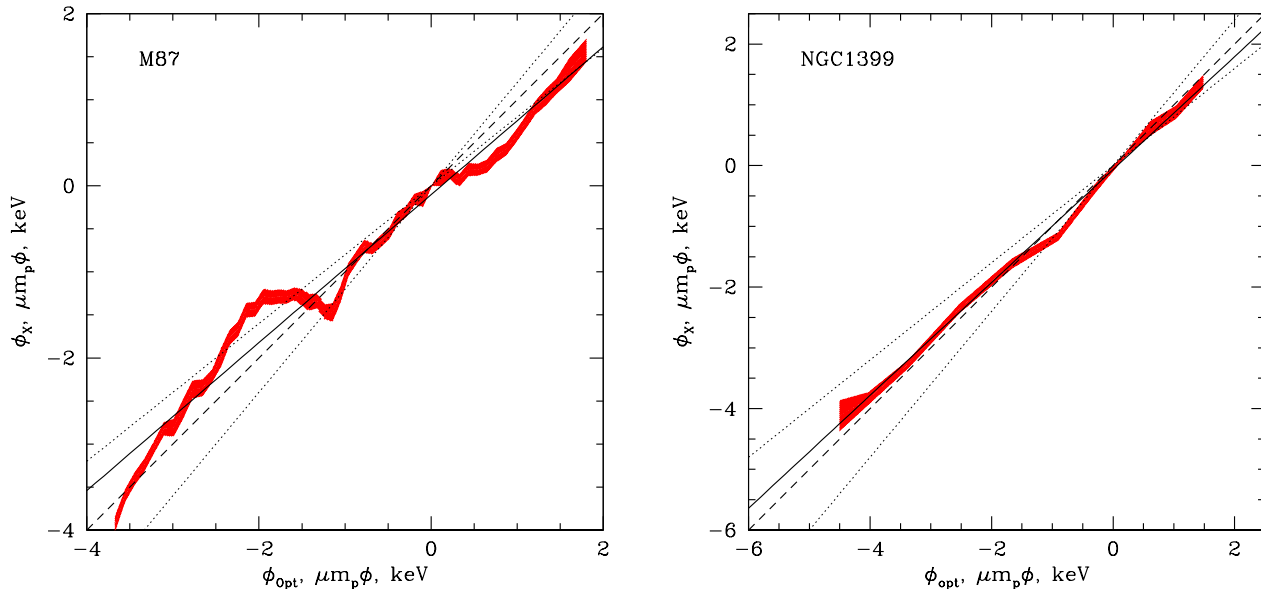


**Figure 9.** Potential derived from X-ray data plotted versus the potential derived from optical data for M87 and NGC 1399 (red shaded areas). The thick solid line is a formal linear fit  $\varphi_X = a\varphi_{opt} + b$ . The values of  $a$  are 0.85 and 0.93 for M87 and NGC 1399 respectively. The thick dashed line shows the dependence  $\varphi_X = \varphi_{opt}$ , while thin dotted lines correspond to  $a=0.8$  and  $1.2$ .

re-heating is the activity of the central supermassive black hole, mediated by the outflow of relativistic plasma. Actual gas heating might be due to dissipation at shock fronts (e.g., David et al. 2001) or in sound waves (if the medium is viscous, has appreciable thermal conductivity or is strongly non-uniform, e.g., Fabian 2003, 2005; Heinz & Churazov 2005; Ruszkowski et al. 2004a, 2004b) or may go through the intermediate step of turbulence generation, which eventually dissipates its energy (e.g., Churazov et al. 2001, 2002). We now test whether our results on the non-thermal forms of pressure are consistent with this picture.

First, we directly see bubbles of relativistic plasma (as radio bright regions and as ‘cavities’ in X-rays). If the M87 gas is in a quasi-equilibrium state with cooling losses, on average compensated by heating, then the mechanical power of the outflow should be related to the gas cooling losses. As argued in Churazov et al. (2001), Begelman (2001), and Nulsen et al. (2006), the efficiency of energy transfer from relativistic outflow to the gas is high when the outflow subsonically crosses regions with large pressure gradients. In this case, one can simply assume that the power of the outflow is equal to the cooling losses. The total energy of the bubbles of relativistic plasma in the region can then be estimated from the balance of powers as  $\mathcal{E}/t_{cross} \sim \mathcal{E}_{thermal}/t_{cool}$ , where  $\mathcal{E}_{thermal}$  is the gas thermal energy,  $t_{cool}$  is the gas cooling time and  $t_{cross}$  is the time each bubble spends inside the region where it deposits a significant fraction of its enthalpy. For instance, consider a 10 kpc region around M87. For an electron density  $n_e = 2 \cdot 10^{-2} \text{ cm}^{-3}$  and a temperature  $T_e = 1.7 \text{ keV}$ , the cooling time  $t_{cool} \sim 4 \cdot 10^8 \text{ yr}$ . On the other hand, the rise velocity of large buoyantly driven bubbles is  $\zeta c_s$  where  $c_s$  is the sound speed and  $\zeta$  is the factor of order 0.5 (e.g., Churazov et al. 2001). Thus  $t_{cross} \approx 3 \cdot 10^7 \text{ yr}$  for

the 10 kpc region. Therefore, bubbles of relativistic plasma should, on average, account for a fraction  $t_{cross}/t_{cool} \sim 0.1$  of the total energy (or volume). This is consistent with the results we obtained from Fig. 9. Of course, the above estimate is probably accurate only to within a factor of few.

We can now check whether our limits exclude turbulence as an intermediate reservoir of energy in the process: moving bubbles  $\rightarrow$  turbulence  $\rightarrow$  viscous dissipation and gas heating as suggested by Chandran (2004) and Rebusco et al. (2005, 2006). In this case, the energy dissipation rate of the turbulent motions should be approximately equal to the gas cooling losses:

$$C \mu m_p n \frac{v_{turb}^3}{l_{turb}} \approx \frac{3/2nkT}{t_{cool}}, \quad (16)$$

where  $v_{turb}$  and  $l_{turb}$  are the characteristic velocity and spatial scale of energy containing eddies,  $n$  is the gas particle density and  $C$  is a dimensionless constant of the order of unity. According to a recent compilation by Dennis & Chandran (2005),  $C \sim 0.42$ . If the energy in the micro-turbulence is constrained to be less than a fraction  $\xi$  of the thermal energy, then

$$\frac{1}{2} \mu m_p n v_{turb}^2 \lesssim \xi \frac{3}{2} nkT, \quad (17)$$

and then

$$\frac{v_{turb}}{l_{turb}} \gtrsim \frac{1}{2C} \frac{1}{\xi} \frac{1}{t_{cool}}. \quad (18)$$

Therefore  $v_{turb} \gtrsim 20 \left( \frac{l_{turb}}{1 \text{ kpc}} \right) \left( \frac{\xi}{0.15} \right)^{-1} \text{ km s}^{-1}$ . This condition is likely satisfied in the gas around M87 (if it is indeed turbulent) since the characteristic size of individual bubbles

is of order 1–3 kpc and their velocities are expected to be significantly higher, a few  $10^2 \text{ km s}^{-1}$  (Churazov et al. 2001).

Thus, our constraints on the non-thermal pressure support do not contradict the current paradigm of cooling flows, which assumes a balance between radiative cooling and mechanical heating of the gas. On the other hand, our conclusion that the fraction of the energy density in the form of cosmic rays and magnetic fields is  $\lesssim 10\text{-}20\%$  provides a non-trivial constraint on the history of the ICM. In particular, these limits apply to the mixing of thermal plasma with relativistic plasmas, the generation of cosmic rays by shocks in the bulk of the ICM, etc. It is in general believed that the energy density of cosmic rays is dominated by protons rather than electrons and the particles with the lowest  $\gamma$  provide the most important contribution to the energy density. The life time of a transrelativistic proton ( $\gamma = 2$ ) with respect to Coulomb energy losses in a cluster plasma with electron density of  $10^{-2} \text{ cm}^{-3}$  is of order of 5 Gyr. Therefore, the energy density of relativistic protons is largely conserved (except for adiabatic losses) during the life time of the cluster (transrelativistic electrons have of course much shorter life times). This implies that our constraints on the energy density of cosmic rays in the cores of M87 and NGC 1399 today actually limit the presence of relativistic protons during the entire history of the same gas lump, provided that relativistic particles are not able to diffuse out of the lump. The constraints on cosmic ray energy density in the past may be even tighter if cosmic rays were originally deposited into a gas lump which had much higher entropy than is observed today and has lost the excess entropy by cooling. Indeed, if relativistic protons experience only adiabatic losses, then their energy density  $\varepsilon_{CR}$  changes with gas density as:

$$\varepsilon_{CR,1} = \varepsilon_{CR,0} \left( \frac{\rho_{gas,1}}{\rho_{gas,0}} \right)^{\gamma_{CR}}, \quad (19)$$

while the thermal energy is by definition

$$\varepsilon_{gas,1} = \varepsilon_{gas,0} \left( \frac{\rho_{gas,1} T_{gas,1}}{\rho_{gas,0} T_{gas,0}} \right). \quad (20)$$

Thus

$$\frac{\varepsilon_{CR,1}}{\varepsilon_{gas,1}} = \frac{\varepsilon_{CR,0}}{\varepsilon_{gas,0}} \times \left( \frac{\rho_{gas,1}}{\rho_{gas,0}} \right)^{\gamma_{CR}-1} \frac{T_{gas,0}}{T_{gas,1}}. \quad (21)$$

Therefore, any constraint on the energy density of cosmic rays now  $\frac{\varepsilon_{CR,0}}{\varepsilon_{gas,0}} \lesssim 0.2$ ,  $\frac{\varepsilon_{CR,0}}{\varepsilon_{gas,0}} \lesssim 0.1$  for M87 and NGC 1399 respectively, can be transformed into constraints on the  $\frac{\varepsilon_{CR,1}}{\varepsilon_{gas,1}}$  in the same gas lump. This is illustrated in Fig. 10. Solid and open squares show the gas density and temperature observed in the cores of M87 and NGC 1399 today. Along the thick solid line ( $T \propto \rho^{\gamma_{CR}-1}$ ) the ratio  $\frac{\varepsilon_{CR,1}}{\varepsilon_{gas,1}}$  is constant. Therefore if the gas lump we see now in the core of NGC 1399 had in the past the density and the temperature along this line, then the constraint on the energy density of cosmic rays was the same as now:  $\frac{\varepsilon_{CR,1}}{\varepsilon_{gas,1}} \lesssim 0.1$ . Thin solid lines show the parameters for which present day constraints transform into a  $\frac{\varepsilon_{CR,1}}{\varepsilon_{gas,1}}$  limits of 0.01 and 1 respectively. For comparison, we show a few typical states of the IGM/ICM, ranging from warm gas in sheets and filaments (triangle symbols and the dash-dotted line) of the Large Scale Structure to shock heated gas in galaxy clusters (dotted curves). The cluster data are taken from simulations of Nagai, Vikhlinin & Kravtsov (2007) for  $z = 0$ . The data for 3 keV and 8

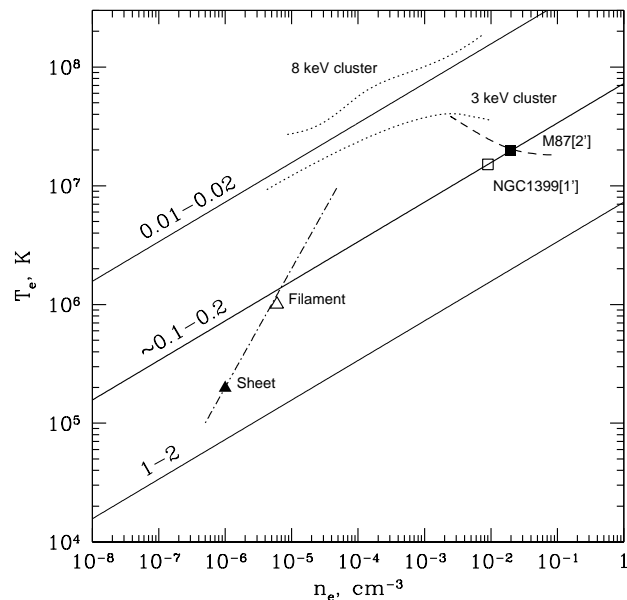


**Figure 10.** Constraints on the energy density of cosmic rays during the evolution of gas lumps presently seen in the cores of M87 and NGC 1399. The ratio  $\frac{\varepsilon_{CR,1}}{\varepsilon_{gas,1}}$  is constant along the solid lines. If the gas had in the past a density and temperature along the thick solid line, then at that time the constraint on energy density of cosmic rays is the same as now:  $\frac{\varepsilon_{CR,1}}{\varepsilon_{gas,1}} \lesssim 0.1$ . Thin solid lines show the parameters for which present day constraints transform into  $\frac{\varepsilon_{CR,1}}{\varepsilon_{gas,1}}$  limits of 0.01 and 1, respectively. For comparison we show a few typical states of the IGM/ICM, ranging from warm gas in sheets and filaments (triangle symbols and the dash-dotted line) of the large scale structure to shock-heated gas in galaxy clusters (dotted curves). The dashed line shows the locus of  $(n_e, T_e)$  points taken from radially averaged profiles of the ICM in M87 at distances from  $0'.5$  to  $5'$  from the center.

keV clusters were used and radial profiles plotted in Fig. 10 correspond to distances from  $\sim 70$  kpc to  $\sim 2$  Mpc from the cluster center. The main conclusion of this simple exercise is that if the gas in the core of M87 or NGC 1399 were in the past shock heated above the upper solid line, the energy density of cosmic rays in the gas was at that time less than 1-2% of the thermal energy density. We emphasize again that this conclusion is based on the assumption that cosmic rays dominating the energy density (presumably low energy protons) are not able to diffuse out of the gas lump and they suffer only from adiabatic losses. Allowing diffusion would essentially imply that our upper limits are applicable to the moment of observations only.

Gamma-ray observations of clusters (Reimer et al. 2003) do limit the presence of cosmic rays, in particular protons, to less than  $\sim 20\%$  of the gas thermal energy (e.g., Pfrommer & Ensslin 2004). It is interesting that Brunetti et al. (2007) have recently derived an upper limit on the contribution of relativistic protons to the gas pressure based on radio observations (upper limits) of clusters without radio halos. While the actual limit on protons is sensitive to the assumed strength of the magnetic field for many clusters it falls below

1% (for  $> \mu G$  field) of the thermal pressure measured from the X-ray gas.

X-rays can be used to constrain mass/potential profiles of elliptical galaxies as long as the galaxy is gas rich and the contribution of individual stellar-mass systems to the X-ray emission (e.g., Revnivtsev et al. 2007) can be neglected. This implies that the X-ray analysis can be applied to massive ( $\gtrsim 10^{11} M_{\odot}$ ) systems. The most massive ellipticals often dwell at the centers of groups/clusters (like NGC1399 and M87) and then X-rays can be used over a broad range of radii from a fraction of the central galaxy effective radius to distances almost comparable to the cluster virial radius. The optical data on stellar kinematics are mostly useful up to 1-2  $R_e$ . This range of radii can be extended to a few  $R_e$  with tracers such as globular clusters and planetary nebula (e.g., Samurovic & Danziger 2006, Wu & Tremaine 2006), and to much larger radii using satellite galaxies or weak gravitational lensing. The comparison of lensing and X-ray masses made by Mahdavi et al. (2007) for a sample of 18 clusters yielded  $M_X/M_L = 1.03 \pm 0.07$  and  $M_X/M_L = 0.78 \pm 0.09$  at radii corresponding to overdensities of 2500 and 500 respectively. These results, characterizing cluster properties at radii  $\sim 0.3-1.5$  Mpc, are broadly consistent with our findings for the inner few tens of kpc. When combined with our work, these results suggest that the contribution of non-thermal components to pressure does not exceed  $\sim 10-20\%$  over the entire cluster volume, as long as the system has not recently experienced a major merger. In numerical simulations of structure formation there is a substantial (few per cent - tens of percent) contribution from residual stochastic gas motions to the pressure (e.g., Evrard 1990; Nagai, Vikhlinin & Kravtsov 2007), especially in the outer regions of clusters. If one accounts for this apparently unavoidable contribution, the remaining room for cosmic rays and magnetic fields shrinks further, to  $\leq 10\%$  over the whole cluster volume. Note however that the conditions in the cluster outskirts and core are markedly different and it is unlikely that a universally applicable limit can be easily derived.

## 7 CONCLUSIONS

Using Chandra observations of M87 and NGC 1399 we derive the gravitational potential profiles of these galaxies and compare them with the potentials derived from optical data. Both the X-ray and optical methods – one based on the hydrostatic equilibrium of hot gas and the other on stellar dynamics – give consistent profiles to within  $\sim 10-20\%$  over a broad range of radii (factor of 30–100). In M87, several obvious wiggles in the X-ray derived profile can plausibly be attributed to a spherical shock propagating through the ICM.

These results suggest that the combined contribution of cosmic rays, magnetic fields and micro-turbulence must be less than 7-15% of the gas thermal energy (with conservative upper limits of 10 and 20% for NGC 1399 and M87 respectively). These findings are consistent with the current paradigm of cool cluster cores, based on the assumption that AGN activity regulates the thermal state of the gas by injecting energy into the ICM.

The limit of  $\sim 10-20\%$  on the energy density, in the form of relativistic protons, applies not only to the current state

of the gas, but essentially to the entire history of the ICM, provided that cosmic ray protons evolve adiabatically and their spatial diffusion is suppressed.

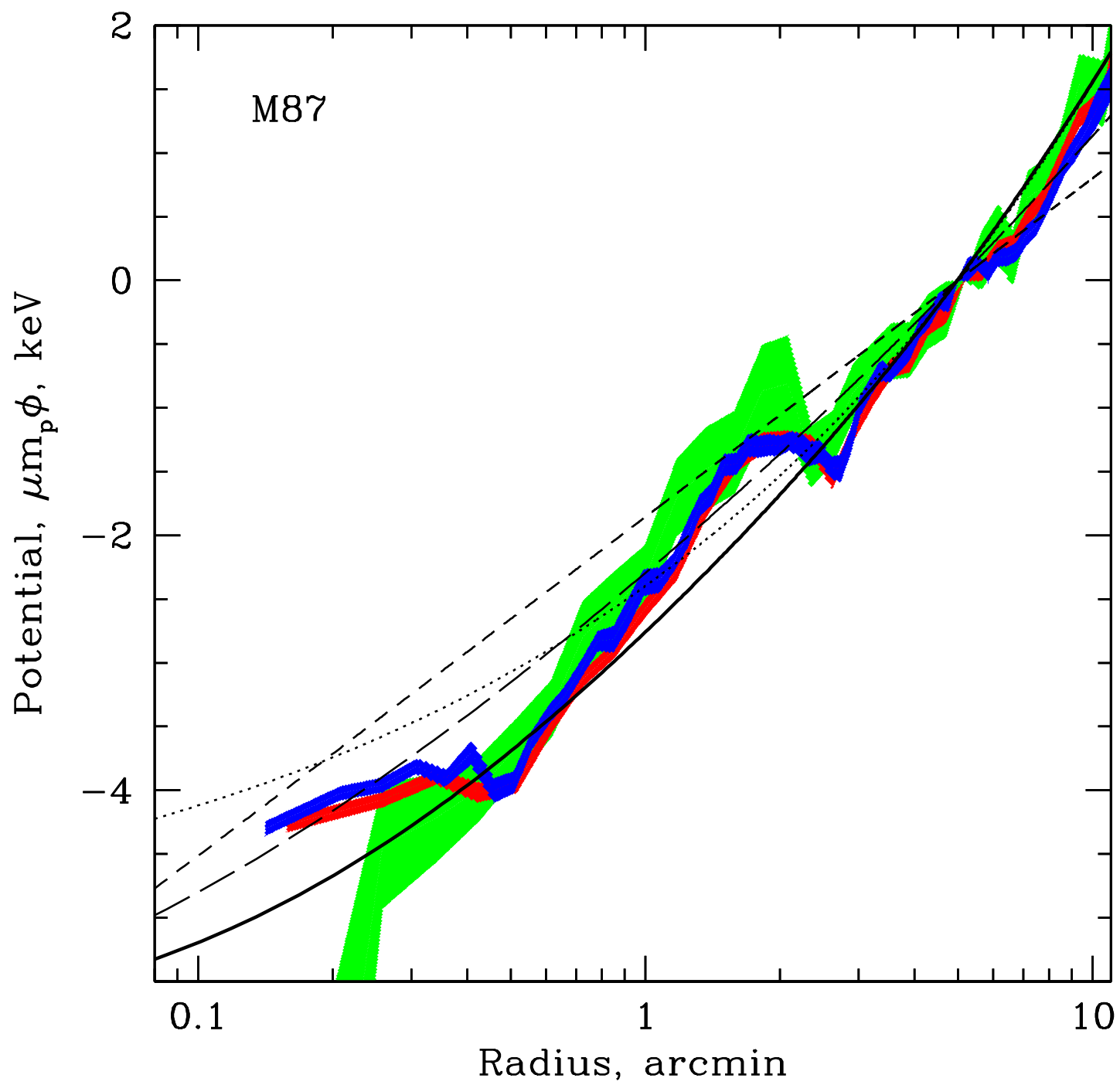
## 8 ACKNOWLEDGEMENTS

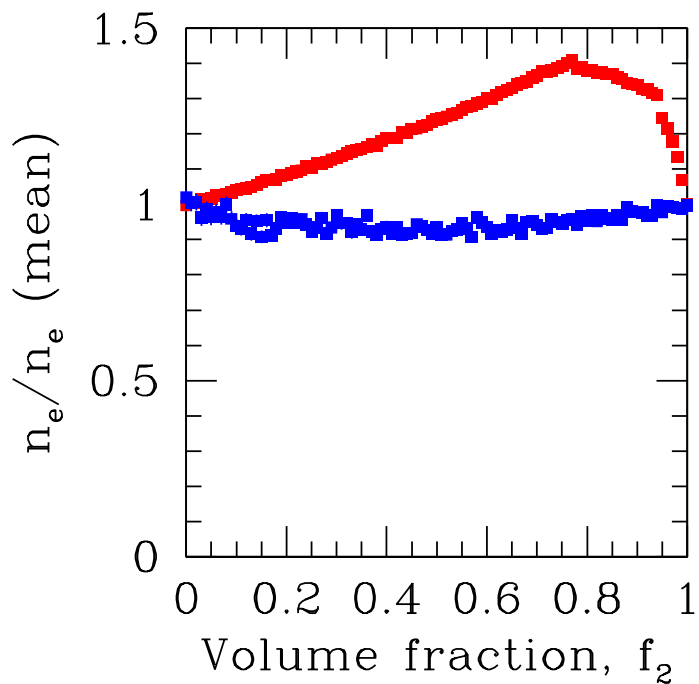
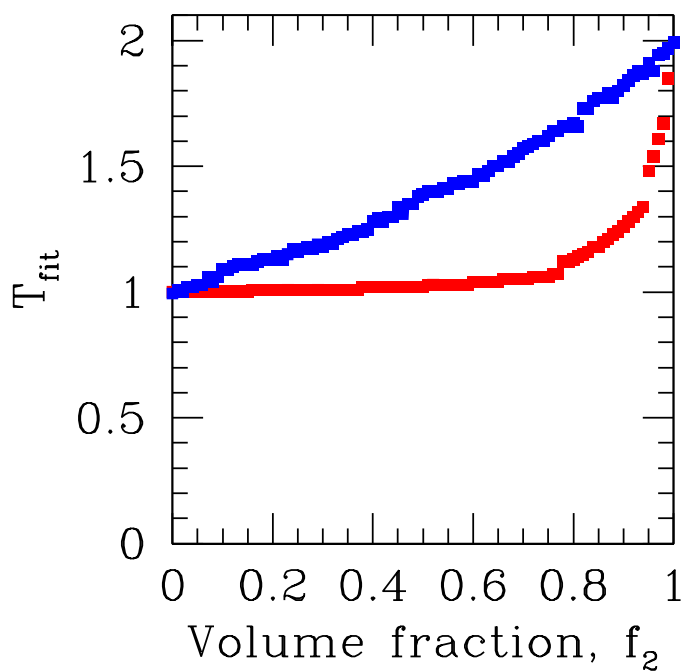
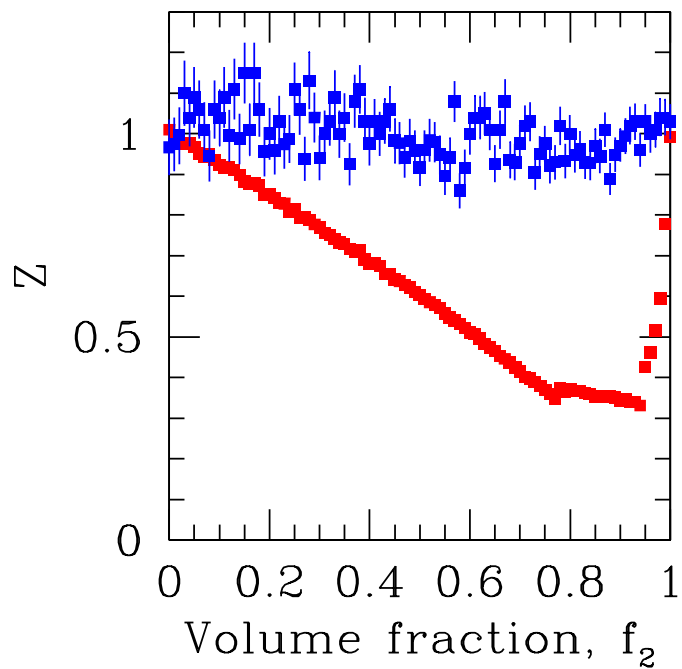
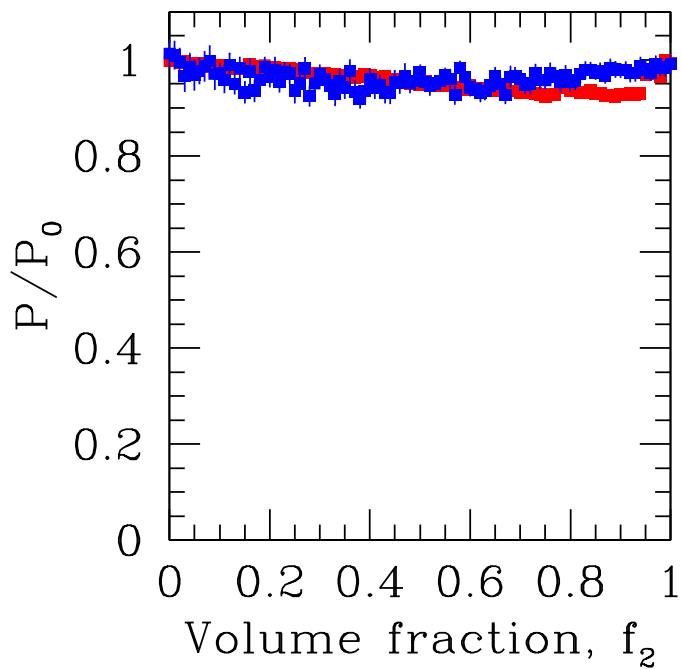
This work was supported by the DFG grant CH389/3-2, NASA contracts NAS8-38248, NAS8-01130, NAS8-03060, the Chandra Science Center, the Smithsonian Institution, MPI für Astrophysik, and MPI für Extraterrestrische Physik. ST acknowledges support from a Humboldt Research Award.

## REFERENCES

- Arnaud K. A., 1996, ASPC, 101, 17  
 Begelman M. C., 2001, ASPC, 240, 363  
 Belsole E. et al. 2001, A&A, 365, L188  
 Binney J., Tremaine S., 1987, Galactic Dynamics, Princeton Univ. Press, Princeton, NJ  
 Böhringer H. et al., 2001, A&A, 365, L181  
 Böhringer H. Neumann, D. M., Schindler, S., Huchra, J. P., 1997, ApJ, 485, 439  
 Brunetti G., Venturi T., Dallacasa D., Cassano R., Dolag K., Giacintucci S., Setti G., 2007, ApJ, 670, L5  
 Buote D. A., 2000, ApJ, 539, 172  
 Chandran B.D.G., 2004, ApJ, 616, 169  
 Churazov E., Gilfanov M., Forman W., Jones C., 1996, ApJ, 471, 673  
 Churazov E., Brüggem M., Kaiser C. R., Böhringer H., Forman W., 2001, ApJ, 554, 261  
 Churazov E., Sunyaev R., Forman W., Böhringer H., 2002, MNRAS, 332, 729  
 Churazov E., Forman W., Jones C., Böhringer H., 2003, ApJ, 590, 225  
 Churazov E., Forman W., Jones C., Sunyaev R., Böhringer H., 2004, MNRAS, 347, 29  
 David L. P., Nulsen P. E. J., McNamara B. R., Forman W., Jones C., Ponman T., Robertson B., Wise M., 2001, ApJ, 557, 546  
 Dickey J. M., Lockman F. J., 1990, ARA&A, 28, 215  
 Diehl S., Statler T. S., 2007, ApJ, 668, 150  
 Dirsch B., Richler T., Geisler D., Forte J. C., Bassino L. P., Gieren, W. P., 2003, AJ, 125, 1908  
 Dennis T. J., Chandran B. D. G., 2005, ApJ, 622, 205  
 Evrard A. E., 1990, ApJ, 363, 349  
 Fabian, A., Sanders, J., Allen, S., Crawford, C., Iwasawa, K., Johnstone, R., Schmidt, R., Taylor, G. 2003, MNRAS, 344, L43  
 Fabian, A., Reynolds, C., Taylor, G., Dunn, R. 2005, MNRAS, 363, 891  
 Fabricant D., Gorenstein P., 1983, ApJ, 267, 535  
 Forman, W., Jones, C., Tucker, W., 1985, ApJ, 293, 102  
 Forman W. et al., 2005, ApJ, 635, 894  
 Forman W. et al., 2007a, ApJ, 665, 1057  
 Forman W. et al., 2007b, ApJ, to be submitted  
 Fukazawa, Y., Botoya-Nonesu, J. G., Pu, J., Ohto, A., Kawano, N., 2006, ApJ, 636, 698  
 Gorenstein P., Fabricant D., Topka K., Tucker W., Harnden F. R., 1977, ApJ, 216, L95

- Heinz, S., Churazov, E., 2005, *ApJL*, 634, L141
- Humphrey, P., Buote, D., Gastaldello, F., Zappacosta, L., Bullock, J., Brighenti, F., Mathews, W., 2006, *ApJ*, 646, 899
- Kronawitter A., Saglia R. P., Gerhard O., Bender R., 2000, *A&AS*, 144, 53
- Lokas E. L., Mamon G. A., 2003, *MNRAS*, 343, 401
- Mahdavi A., Hoekstra H., Babul A., Henry J. P., 2007, arXiv:0710.4132
- Markevitch M. et al., 2000, *ApJ*, 541, 542
- Markevitch, M. 2001, Chandra calibration memo, <http://asc.harvard.edu/cal/>, “ACIS,” “ACIS Background” and <http://xc.harvard.edu/contrib/maxim/acisbg/COOKBOOK>
- Matsushita K., Belsole E., Finoguenov A., Böhringer H., 2002, *A&A*, 386, 77
- Mathews, W. 1978, *ApJ*, 219, 413
- McLaughlin D. E., 1999, *AJ*, 117, 2398
- Nagai D., Vikhlinin A., Kravtsov A. V., 2007, *ApJ*, 655, 98
- Navarro J. F., Frenk C. S., White S. D. M., 1996, *ApJ*, 462, 563
- Nulsen, P. E. J., Jones, C., Forman, W., David, L., McNamara, B., Rafferty, D., Birzan, L., Wise, M., 2006, in Böhringer H., Schuecker P., Pratt G. W., Finoguenov A., eds, *Heating vs. Cooling in Galaxies and Clusters of Galaxies*. Springer-Verlag, Berlin (astro-ph/0611136)
- Nusser A., Silk J., 2007, arXiv, 711, arXiv:0711.1281
- Peterson J. R., Kahn S. M., Paerels F. B. S., Kaastra J. S., Tamura T., Bleeker J. A. M., Ferrigno C., Jernigan J. G., 2003, *ApJ*, 590, 207
- Pfrommer C., Enßlin T. A., 2004, *A&A*, 413, 17
- Rebusco P., Churazov E., Böhringer H., Forman W., 2005, *MNRAS*, 359, 1041
- Rebusco P., Churazov E., Böhringer H., Forman W., 2006, *MNRAS*, 372, 1840
- Reimer O., Pohl M., Sreekumar P., Mattox J. R., 2003, *ApJ*, 588, 155
- Revnivtsev M., Churazov E., Sazonov S., Forman W., Jones C., 2007, *A&A*, 473, 783
- Reynolds, C., Heinz, S., Begelman, M. 2001, *ApJL*, 549, 179
- Romanowsky A. J., Kochanek C. S., 2001, *ApJ*, 553, 722
- Ruszkowski M., Brügggen M., Begelman M.C., 2004a, *ApJ*, 611, 158
- Ruszkowski M., Brügggen M., Begelman M.C., 2004b, *ApJ*, 615, 675
- Saglia R. P., Kronawitter A., Gerhard O., Bender R., 2000, *AJ*, 119, 153
- Samurović S., Danziger I. J., 2006, *A&A*, 458, 79
- Smith R. J., Lucey J. R., Hudson M. J., Schlegel D. J., Davies R. L., 2000, *MNRAS*, 313, 469
- Smith R. K., Brickhouse N. S., Liedahl D. A., Raymond J. C., 2001, *ApJ*, 556, L91
- Thomas J., Saglia R. P., Bender R., Thomas D., Gebhardt K., Magorrian J., Corsini E. M., Wegner G., 2007, arXiv:0709.0691
- Wu X., Tremaine S., 2006, *ApJ*, 643, 210





## 0.1 Uniform medium

$$\varphi_{true} = - \int \frac{1}{\rho_{true}} \frac{dP_{true}}{dr} dr, \quad (1)$$

where  $\varphi_{true}, \rho_{true}, P_{true}$  - true potential, mean mass density and total pressure.

We measure:  $\varphi_X, \rho_X, T_X$  and  $P_X = \rho_X T_X$  - derived from X-ray data - potential, density, temperature and pressure (I dropped  $k, \mu, m_p$  from all expressions).

For uniform density case we assume  $\rho_X = \rho_{true}$  and  $P_X = f_g P_{true}$ . Then

$$\varphi_X = - \int \frac{1}{\rho_X} \frac{dP_X}{dr} dr = \quad (2)$$

$$- \int \frac{1}{\rho_{true}} \frac{df_g P_{true}}{dr} dr = \quad (3)$$

$$- \int f_g \frac{1}{\rho_{true}} \frac{dP_{true}}{dr} dr - \int \frac{P_{true}}{\rho_{true}} \frac{df_g}{dr} dr = \quad (4)$$

$$\int f_g \varphi_{true} - \int \frac{P_X/f_g}{\rho_X} \frac{df_g}{dr} dr = \quad (5)$$

$$\int f_g \varphi_{true} - \int T_X \frac{d \ln f_g}{dr} dr \quad (6)$$

The  $\ln f_g$  appears because I assume that  $\frac{P}{\rho} \equiv \frac{P_{true}}{\rho_{true}} = \frac{P_X/f_g}{\rho_X} = \frac{T_X}{f_g}$  instead of simply  $T_X$ . May be I shall change the notations in the text?

## 0.2 Patchy medium

Here I assume that:

$$\rho_X = \rho_{true} / \sqrt{f_g} = \rho_{gas} \sqrt{f_g} \quad (7)$$

$$P_X = T_X \rho_X = P \sqrt{f_g}. \quad (8)$$

Then

$$\varphi_X = - \int \frac{1}{\rho_X} \frac{dP_X}{dr} dr = \quad (9)$$

$$- \int \frac{1}{\rho_{true}} \sqrt{f_g} \frac{d \sqrt{f_g} P_{true}}{dr} dr = \quad (10)$$

$$\int f_g \varphi_{true} - \int \frac{T_X}{\sqrt{f_g}} \frac{\sqrt{df_g}}{dr} dr = \quad (11)$$

$$\int f_g \varphi_{true} - \frac{1}{2} \int T_X \frac{d \ln f_g}{dr} dr \quad (12)$$

